Light Water Reactor Sustainability Program

Microstructural Characterization of Reactor Pressure Vessel Alloys: ATR-2 Experiment Update

September 2017

U.S. Department of Energy

Office of Nuclear Energy

Microstructural Characterization of Reactor Pressure Vessel Alloys: ATR-2 Experiment Update

G. R. Odette, T. Yamamoto, P. Wells, N. Almirall and D. Gragg

September 2017

Prepared for the
U.S. Department of Energy
Office of Nuclear Energy

Contents

Figures

Tables

Acknowledgements

This research was supported by the DOE NSUF, NEUP and LWRS (via ORNL) programs. We wish to acknowledge many individuals who have contributed to this work. First the ATR-2 irradiation was made possible by the Nuclear Science User Facilities and the outstanding team of scientists, engineers and managers at the Idaho National Lab led by Michel Meyer, and including Michael Sprenger, Paul Murray, Joseph Nielson, Collin Knight, Thomas Maddock, Dan Ogden, James Cole, Todd Allen and Rory Kennedy. Other major contributors include Keith Wilford and Tim Williams at Rolls Royce. This work is being carried out in close collaboration with Keith Leonard, Randy Nanstad, Janet Robertston, Michael Sokolov, Frank Chen and Phil Edmondson at ORNL, William Server at ATI Consulting, Lynne Ecker and David Sprouster at BNL and Naoki Soneda at CRIEPI. Rolls Royce provided the advanced steel matrix alloys for this experiment. NIST provided the SANS facilities and John Barker has contributed significantly in helping us to conduct these experiments. We would also like to acknowledge the Center for Advanced Energy Studies (CAES) Microscopy and Characterization Suite (MaCS) where the sample preparation for Atom Probe Tomography was carried out with the assistance of Jatu Burns, Allyssa Bateman and Joanna Taylor. Many other individuals at UCSB also contributed most notably Kirk Fields, Doug Klingensmith, Nicholas Cunningham and Yuan Wu. Finally we would like to acknowledge many fruitful discussions with Dane Morgan's group at the University of Wisconsin.

Executive Summary

The overarching goal of the UCSB ATR-2 irradiation program is to provide foundational microstructural and mechanical property databases for developing new physical models to accurately predict embrittlement of reactor pressure vessel steels at high fluence for extended life operation. The ATR-2 irradiation was carried out in the Advanced Test Reactor at the Idaho National Laboratory, supported by the National Scientific User Facilities Program. The UCSB ATR-2 test train irradiated 1625 specimens of various types, representing 172 alloys, over a range of flux (ϕ), fluence (ϕt) and temperature (T). The irradiation has a peak ϕ of 3.6×10^{12} n/s-cm^2, which is $\approx$ 10 times the maximum level in the surveillance database, and $\approx$ 70 times higher than for PWR vessel service. The corresponding peak $\phi t \approx 1.4 \times 10^{20}$ n/cm^2 is about 40% larger than will be reached by some vessels in 80 years of operation. ATR-2 was designed to provide an intermediate flux bridge connecting very large existing embrittlement databases developed by UCSB and others that encompass low flux surveillance to very high flux test reactor flux conditions.

Here we provide a status report on the ATR-2 program microstructural characterization task. Previous reports [1, 2] have shown that embrittlement at 1.4×10^{20} n/cm^2 and 290°C, as manifested by irradiation hardening, is generally systematically and significantly under-predicted by current regulatory models, including both the Eason-Odette-Nanstad-Yamamoto (EONY) model [3] and the more recent American Society for Testing and Materials (ASTM) E900 Standard [4]. Further, previous microstructural characterization, by atom probe tomography (APT) and small angle neutron scattering (SANS), showed that the high fluence hardening includes significant contributions from both copper rich precipitates (CRPs) in Cu bearing steels, and so-called late blooming phases (LBP), in the form of nano-scale Mn-Ni-Si precipitates (MNSPs) in both low Cu (< 0.07 wt.%), and Cu bearing alloys [5]. The CRPs

quickly from and grow to saturation due to depletion of the dissolved matrix Cu. MNSP LBP emerge only at higher fluence in steels with intermediate and high Ni contents. The mole fractions (f) of MNSPs can be much larger than that CRPs, since RPV steels contain much more Mn + Ni + Si alloying elements, typically up to 3.5 wt.%, compared to impurity Cu at < 0.4 wt.%. Note irradiation hardening roughly scales with the √f.

The combined embrittlement databases address two key questions: a) "when (flux and fluence), where (alloy compositions) and how much (f) do MNSPs contribute to irradiation hardening, involving the combined effects of alloy chemistry, ϕ, ϕt and T; and, b) the effects of ϕ, or dose rate, that must be understood so that that data collected at higher ϕ can be extrapolated to low ϕ service conditions. Answers to the questions will provide the basis for developing a new high fluence-low flux embrittlement model. In addition, UCSB ATR-2 will provide: (a) a test of the validity of the Master Curve fracture toughness assessment method in highly embrittled steels; (b) a large database on post irradiation annealing, including providing a foundation for developing embrittlement remediation methods; and, (c) support for the development of a new class of high Ni advanced RPV alloys.

This report focuses on the evolution CRPs and MNSPs in representative alloys with special emphasis on the peak flux condition (3.6×10^{12} n/s-cm^2) at ≈ 290°C as a function of alloy composition. A smaller subset of data has also been recently acquired on the so-called advanced steel matrix (ASM) alloys, which include very high Ni steels, irradiated at ≈ 250°C.

Key findings are summarized in the following bullets:

- The total precipitate f grows continuously in low Cu steels, first slowly as solute clusters form as stable matrix feature (SMF) defect complexes in displacement cascades and then, at an accelerated rate as well-formed MNSPs, above a relatively high threshold ϕt.

- In Cu bearing steels, the CRPs first grow rapidly to a saturated plateau f, at dissolved matrix Cu depletion, followed growth of MNSPs at higher fluence.
- The precipitates first grow with a CRP core Mn-Ni-Si shell structure, but the MNSPs later transform to discrete ordered intermetallic appendages at higher fluence.
- The precipitates heterogeneously form on dislocations at lower solute concentrations and higher temperatures (that is lower supersaturation).
- X-ray diffraction (XRD) and Small Angle X-ray Scattering (SAXS) studies have shown that the MNSPs in 5 out of 6 core RPV steels are consistent with an intermetallic G-phase, but that the Γ_2 phase was selected in one Low Cu, high Ni, lower Si steel.
- On average SANS measures ≈2/3 of the APT f
- The total f scales with 3Cu + Ni at lower ϕt in Cu bearing steels, compared to a 2Ni + Cu dependence at very high ϕt. Note these chemistry factors are not optimized.
- In low Cu (< 0.07 wt.%) steels, with typical amounts of Mn (> ≈ 1.0%), the MNSP f is primarily controlled by Ni.
- SANS studies for the 290°C irradiation to 1.4×10^{20} n/cm^2, show f increases with both Cu, due its effect on d, and Ni due to its effect on N.
- The total f is also generally insensitive to variations in Mn at sufficient concentrations (> ≈ 1%) of this element.
- SANS studies 250°C and 290°C irradiations of advanced steel matrix (ASM) alloys, with a much wider than normal range of compositions, including up to ≈ 3.5% Ni, also show f scaling with 3Cu + Ni in alloys with sufficient Mn > 1.5%.

- The f is larger for irradiations at the lower T = 250°C by ≈ 13 and 28% at high and low Mn, respectively.
- The f in low Mn ≈ 0.25% alloys also scales with 3Cu + Ni, but is lower by a factor of ≈ 3, than in the case of higher Mn steels.
- This "Mn starvation" effect opens the way to developing new high performance steels with up to 3.5% Ni that contain Mn $\leq$ 0.3%.
- The large reduction in f at very low Mn is associated with an insufficient amount of this element to form the typical G and Γ_2 phases
- In this case smaller amounts of Ni-silicide MNSPs are sometimes selected in steels with normal Si levels.
- The total f is relatively insensitive to variations in Si and P.
- The evolution of the MNSP f can be described by an Avrami precipitation model, combined with an formation-transformation model for SMF cascade solute-defect clusters starting at very low ϕt, that are precursors to MNSP, In Cu-bearing steels, the evolution of f can be described by two Avrami models for CRPs (core) and MNSP-appendage structures, respectively, plus the SMF cited above.
- The ϕ, or dose rate, effect can be understood and modeled in detail based on enhanced vacancy and self-interstitial atom recombination at solute traps and cascade defect fragments with increasing ϕ.
- The ϕ (dose rate) dependence of the evolution of f with ϕt can be treated in terms of a flux-dependent effective fluence (ϕt_e) that accounts for vacancy and self-interstitial atom recombination. The ϕ dependence of ϕt_e can be approximately treated by a

simple scaling relation as $\phi t_e = \phi t[\phi r/\phi]^p$, where ϕ_r is an arbitrary reference ϕ, and p is an empirical scaling exponent, which is reasonably approximated as $p \approx 0.25$.

- High dose rate ion irradiations produce CRPs and MNSPs that are similar to those found in neutron irradiated steels, and the corresponding f are also similar at high dpa where there is full phase separation..
- Post irradiation annealing (PIA) studies at 425°C for up to 57 weeks show that the MNSPs show that while most MNSPs dissolve, some of the larger ones are stable and begin to coarsen
- PIA at 425°C for 52 weeks of a high Ni steel ion irradiated at 400°C, that initially results in larger precipitates, has little effect on the MNSP, while a population of smaller precipitates MNSPs formed by an initial irradiation at 340°C (followed by a 400°C increment of dpa) coarsen, but do not dissolve.
- These observations show that the MNSPs are equilibrium phases, but ones that can dissolve below a critical radius in a solute depleted matrix.
- The microstructural data can be quantitatively linked to changes in mechanical properties including $\Delta\sigma_y$ and ΔT.
- To first order, $\Delta\sigma_y$ simply correlates with the $\sqrt{f}$, and can be modeled by properly treating strengthening superposition effects.
- This large database of microstructural observations developed in this work formed the foundation for developing detailed thermo-kinetic models of precipitation in RPV steels under irradiation in a strong collaboration between UCSB and the University of Wisconsin.

- Perhaps the most significant remaining challenge is to refine and verify flux effects models that can be applied to analyzing the large surveillance database and to reliably predict embrittlement for low flux-high fluence extended life service conditions.

1. Introduction and Overview

The rapid failure of the massive reactor pressure vessel (RPV) in a light-water reactor (LWR) is beyond a design basis accident, thus regulations require conservative fracture safe margins under both normal operation and accident conditions[a]. Demonstrating such safety margins requires that the fracture toughness of the vessel steel be conservatively greater than any possible in service loads that could propagate postulated cracks. In the unirradiated condition, RPV steels have high fracture toughness levels and vessel fracture is implausible under any postulated condition. However, in-service neutron irradiation degrades the fracture toughness of a RPV steels. Irradiation embrittlement depends on the combination of the sensitivity of the steel, controlled by compositional and starting microstructure metallurgical variables, and the irradiation condition, characterized by the flux (ϕ), fluence (ϕt) and irradiation temperature (T). In-service embrittlement effects are usually quantified by shifting an unirradiated temperature dependent cleavage fracture toughness curve, for a vessel specific steel, by a temperature increment (ΔT), traditionally measured by a corresponding shift in a Charpy V-notch (CVN) impact test energy temperature curves. However, embrittlement can be related to irradiation hardening, typically represented by changes in the yield stress ($\Delta\sigma_y$). The $\Delta\sigma_y$ can be evaluated using tensile, hardness and shear punch tests. More recently, the ΔT for fracture toughness as a function of temperature, in the form of a so-called Master Curve, have been directly measured and used to directly evaluate the ΔT for toughness. Irradiation induced reductions in CVN upper shelf energy, or ductile tearing toughness also occur. Here we focus on developing accurate methods for predicting ΔT based on irradiation hardening for low ϕ, high ϕt extended life conditions.

a. In order to allow time for preparing this report with a focus on the data that we have acquired, along with a first cut analysis and evaluation, we have not included extensive references here, except as specifically needed

Unfortunately there is little data in this ϕ-ϕt regime. Thus the main objective of ATR-2 program is to create and analyze a high ϕt intermediate ϕ database on both mechanical property and microstructural changes in a large number of alloys irradiated over a wide range of conditions. The ATR-2 results will be integrated with a variety of other databases, and used to develop a new high ϕt-low ϕ predictive embrittlement model for extended life, including the effect of T, ϕ, ϕt and alloy composition. Special emphasis is Mn-Ni-Si-Cu late blooming phase (LBP) nano-precipitates, which are observed in a wide range of RPV steels. Our approach is to combine thermo-kinetic models of microstructural evolution with microstructure-property models informed and validated by the combined databases, ultimately including surveillance data, to develop robust models to accurately predict RPV embrittlement at 80 years.

The report is organized as follows. We begin with very brief description of the materials and experimental methods used to obtain the post irradiation examination (PIE) results reported here. The general status of the microstructural PIE is summarized in a master table. The table includes a comprehensive set of synchrotron measurements, but these data have yet analyzed for the most part. The precipitate characterization results are then described in sequence, to illustrate the points in the bulleted list in the executive summary. The report concludes with a very brief note about of future work.

2. **Materials and Methods**

2.1 Materials

ATR-2 contained 172 alloys including: 34 split melt steels with controlled variations in composition that have been previously irradiated in various programs; 23 surveillance steels, including 9 that were acquired specifically for this study; 21 program alloys that generally have also have been previously irradiated; and, 11 simple model alloys for mechanism studies. The

compositions of these alloys are given in [1, 2]. Alloy compositions listed below are all cited in wt.%.

2.2 Irradiation Conditions

The average flux (ϕ), fluence (ϕt) and irradiation temperature (T) both target and as run, for the cups 5, 7, and 8 that contained the alloy conditions that have been microstructurally characterized and reported on here are given in Table 2. Details about how fluxes and temperatures in ATR-2 can be found in the INL as-run reports [6, 7].

Table 2 Neutron ϕ, ϕt (E > 1 MeV) and T for Cups 5, 7 and 8 in the ATR-2 irradiation.

Cup	Flux (10^{12} n/cm^2-s)	Fluence (10^{19} n/cm2)	Target T_{irr} (°C)	Actual T_{irr} (°C)
5	3.36	12.80	250	255
7	3.64	13.90	290	291
8	3.60	13.70	290	293

In addition to the ATR-2 data, we include the results of other UCSB irradiations including the IVAR program, ATR-1 and various piggyback irradiations in the BR2 reactor in Belgium. Further, a number of charged particle irradiations have also been carried out on alloys irradiated in ATR-2, and one illustrative result is shown below. Additional details of the irradiations used to create to overall database that will be used to develop a new embrittlement model will be provided in future reports.

2.3 Microstructural Characterization

Precipitation in the irradiated alloys was characterized using multiple techniques. Descriptions of the various techniques are given elsewhere [1, 2] and will not be repeated here. A total of 28 alloys have been characterized by APT, 69 by SANS, 90 by SAXS and 83 by XRD. A small number of alloys have been also been characterized by various transmission electron microscopy (TEM) techniques. These results, and detailed analysis of the SAXS/XRD database, will be described in future reports. Note, rather extensive characterization has also

been carried out on both ATR-2 and ion irradiated alloys, including in the post irradiation annealed (PIA) condition; some examples are included below. However, the primary focus of this report is on the SANS and APT measurements of ATR-2 alloys from Cup 5, 7 and 8. The status of the PIE on alloys investigated to date is summarized in Tables 2a-c, in terms of mechanical testing (the techniques used are lumped together here), microstructural characterization by various techniques, and the existence of other sources of data on particular steel.

Table 2a Status of characterization in the ASM matrix from ATR-2 Cup 5,7,8

Alloy-Cup	Mech. Testing	Microstructural Characterization				Other
	T/M/S*	APT	SANS	XRD	SAXS	IVAR/BR2/ATR-1**
R1-8	✓	✓	✓	✓	✓	
R1-5	✓		✓	✓		
R2-8	✓			✓	✓	
R2-5	✓					
R3-8	✓				✓	
R3-5	✓					
R4-8	✓		✓	✓	✓	
R4-5	✓		✓			
R5-8	✓			✓	✓	
R5-5	✓		✓	✓		
R6-8	✓			✓	✓	
R6-5	✓		✓	✓		
R7-8						
R7-5	✓		✓	✓		
R8-8	✓			✓	✓	
R8-5	✓			✓		
R9-8	✓			✓	✓	
R9-5	✓			✓		
R10-8	✓		✓	✓	✓	
R10-5	✓		✓	✓		
R11-8	✓			✓	✓	
R11-5	✓					
R12-8	✓				✓	
R12-5	✓					

**Mechanical Testing techniques: Tensile (T), microhardness (M), automated shear punch (S)*

***Irradiation Variables Program, Belgian Reactor 2, Advanced Test Reactor Experiment 1*

R13-8	✓		✓	✓	✓	
R13-5	✓		✓	✓		
R14-8	✓		✓	✓	✓	
R14-5	✓		✓	✓		
R15-8	✓			✓	✓	
R15-5	✓		✓	✓		
R16-8	✓			✓	✓	
R16-5	✓		✓	✓		
R17-8	✓	✓	✓	✓	✓	
R17-5	✓		✓	✓		
R18-8	✓		✓	✓	✓	
R18-5	✓			✓		
R19-8		✓			✓	
R19-5	✓		✓	✓		
R20-8	✓		✓		✓	
R20-5	✓					
R21-8	✓		✓	✓	✓	
R21-5	✓		✓	✓		
R22-8	✓	✓	✓	✓	✓	
R22-5	✓		✓	✓		
R23-8	✓			✓	✓	
R23-5	✓					
R24-8	✓			✓	✓	
R24-5	✓		✓	✓		
R25-8	✓			✓	✓	
R25-5	✓					
R26-8	✓	✓	✓	✓	✓	
R26-5	✓		✓	✓		
R27-8	✓			✓	✓	
R27-5	✓					
R28-8	✓	✓	✓	✓	✓	
R28-5	✓		✓	✓		
R29-8	✓			✓	✓	
R29-5	✓					
R30-8	✓		✓	✓	✓	
R30-5	✓		✓	✓		
R31-8	✓		✓	✓	✓	
R31-5						
R32-8	✓		✓	✓	✓	
R32-5						
R33-8	✓		✓	✓	✓	
R33-5						
R34-8	✓	✓	✓	✓	✓	

R34-5					
R35-8	✓	✓	✓	✓	✓
R35-5					
R36-8	✓			✓	✓
R36-5					
R37-8	✓	✓	✓	✓	✓
R37-5					
R38-8	✓			✓	✓
R38-5					
R39-8	✓		✓	✓	✓
R39-5					
R40-8	✓			✓	✓
R40-5					
R41-8	✓			✓	✓
R41-5					
R42-8	✓		✓	✓	✓
R42-5					
R43-8	✓			✓	✓
R43-5					
R44-8	✓			✓	✓
R44-5					
R45-8	✓				
R45-5					
R46-8	✓				
R46-5					
R47-8	✓		✓	✓	✓
R47-5					
R48-8	✓	✓		✓	✓
R48-5					
R49-8	✓			✓	✓
R49-5					
R50-8	✓		✓	✓	✓
R50-5					
RX1-8				✓	
RX1-5					
RX2-8				✓	
RX2-5					
RX3-8				✓	
RX3-5					
RX4-8				✓	
RX4-5					
RX5-8				✓	
RX5-5					

RX6-8				✓		
RX6-5						
RX7-8				✓		
RX7-5						
RX8-8				✓		
RX8-5						
RX9-8				✓		
RX9-5						
RX10-8	✓			✓	✓	
RX10-5						
RX11-8						
RX11-5						
RX12-8				✓		
RX12-5						
RHA-8	✓			✓	✓	
RHA-5						
RHB-8	✓					
RHB-5						
RHC-8	✓					
RHC-5						
RHD-8	✓					
RHD-5						
RHE-8	✓					
RHE-5						
RHF-8	✓					
RHF-5	✓					

Table 2b Status of characterization in the UCSB SMS matrix from ATR-2 Cup 5,7,8

Alloy-Cup	Mech. Testing	Microstructural Characterization				Other Data
	T/M/S	APT	SANS	XRD	SAXS	IVAR/BR/ATR-1
C1-8						✓
C2-8						✓
C3-8	✓				✓	✓
C4-8	✓					✓
C5-8	✓				✓	✓
C6-8	✓	✓	✓	✓	✓	✓
C7-8	✓		✓		✓	✓
C8-8	✓					✓
C9-8	✓		✓		✓	✓
C10-8	✓					✓
C11-8	✓		✓		✓	✓
C12-8	✓					✓

C13-8	✓		✓			✓
C14-8	✓					✓
C15-8	✓					✓
C16-8	✓		✓		✓	✓
C17-8	✓		✓		✓	✓
C18-8	✓					✓
C19-8	✓		✓		✓	✓
C20-8	✓		✓		✓	✓
C21-8	✓					✓
C22-8	✓		✓		✓	✓
C31-8	✓		✓		✓	✓
LA-8	✓					✓
LB-8	✓			✓	✓	✓
LC-8	✓	✓		✓	✓	✓
LD-8	✓	✓	✓	✓	✓	✓
LJ-8	✓			✓	✓	✓
LK-8	✓					✓
LG-8	✓	✓	✓	✓	✓	✓
LH-8	✓	✓	✓	✓	✓	✓
LP-8	✓					✓
LI-8	✓	✓	✓	✓	✓	✓
LO-8	✓					✓

Table 2c Status of characterization in the Surveillance and Program matrix from ATR-2 Cup 5,7,8

Alloy-Cup	Mech. Testing	Microstructural Characterization				Other Data
	T/M/S	APT	SANS	XRD	SAXS	IVAR/BR/ATR-1
WA-8	✓				✓	✓
WB-8	✓				✓	✓
WC-8	✓				✓	✓
W62-8	✓		✓		✓	✓
W63-8	✓		✓		✓	✓
W65-8					✓	✓
W67-8	✓		✓		✓	✓
W73-8	✓					✓
QC1-8	✓		✓		✓	
QC2-8					✓	
D3-8	✓		✓		✓	
HB-8					✓	
MP-8	✓		✓		✓	
F1W-8	✓	✓	✓		✓	
F2B-8	✓	✓	✓		✓	

KP-8	✓	✓	✓		✓	
MY-8	✓	✓	✓			
BV-8	✓	✓			✓	
KW-8	✓	✓	✓		✓	
F2W-8	✓	✓	✓		✓	
VCW-8	✓	✓	✓		✓	
TP-8	✓	✓			✓	
JRQ-8	✓				✓	✓
EC-8	✓	✓			✓	✓
ED-8	✓	✓				
WM-8	✓					✓
HSST02-8						✓
A302B-8	✓					✓
A508-8	✓					✓
FE	✓	✓				

3. Microstructural Characterization Results Illustrating the Bulleted List of Conclusions Given in the Executive Summary

The characterization results that illustrate the points in the bulleted list in the executive summary section are summarized below.

3.1 Effective Fluence Dependence of f in Cu-free and Cu-Bearing Steels

As illustrated in Figure 1 for low 0.01 %Cu, medium 0.74%Ni steel (LG), the total precipitate f grows continuously in low Cu steels, first slowly as solute defect cluster complexes formed in displacement cascades. These so-called stable matrix features (SMFs) are difficult to observe by SANS measurements that were predominantly used in previous studies mostly at lower fluence. The SMFs transform to well-formed MNSPs and grow at an accelerated and detectable rate above a relatively high threshold ϕt. The left hand figure plots the $\sqrt{f}$ versus the $\sqrt{\phi t_e}$, where ϕt_e is an effective fluence that accounts for flux effects (see below). The figure on the right plots the corresponding change in the yield stress ($\Delta\sigma_y$) versus the square root of the effective fluence that clearly tracks the $\sqrt{f}$ trend, but for many more irradiation conditions, including at low fluence where hardening is due to SMF. The onset of observable precipitation and rapid hardening at more than $\approx 4x10^{19}$ n/cm^2-s is due the MNSP LBP. The large data point is from the ATR-2 irradiation Cup 7 and 8 conditions. The other data points are for a variety of other irradiations at around 290°C for fluxes ranging from $\approx 8x10^{10}$ to $2.2x10^{14}$ n/cm^2-s.

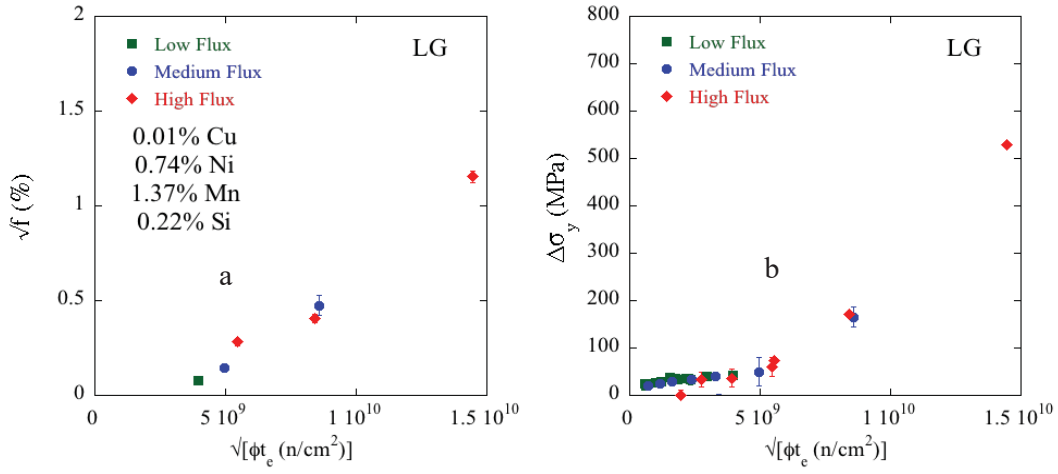

Figure 1 The √f versus root ϕte for a low (0.01%) Cu, medium (0.74%) Ni RPV steel (LG); and, b) the corresponding irradiation hardening.

Figure 2 shows a similar plot for a steel with high bulk 0.41% Cu and high 0.86% Ni (LC). The initial precipitation and hardening transient is due to the CRPs, which grow to near saturation at Cu depletion. The MNSPs evolve more slowly and become increasingly significant at high ϕt.

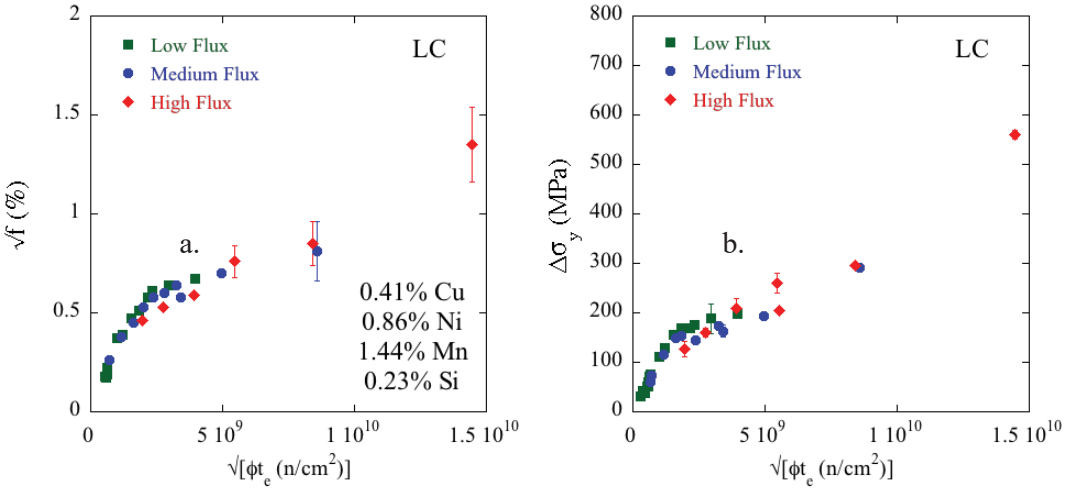

Figure 2 The √f versus root ϕt$_e$ for a high (0.41%) Cu, medium (0.86%) Ni RPV steel (LC); and, b) the corresponding irradiation hardening.

3.2 Characteristics of the 6 UCSB Core Alloys

Figure 3 shows the average diameter (d), number density (N) and mole fraction (f) of the six core alloys in the ATR-2 matrix, with systematic variation in Cu and Ni as function of bulk Cu for medium, high and very high Ni levels. These results are broadly representative of more general trends in the ATR-2 database. The d is roughly constant, while N and f increase with Ni. In all cases Ni is the primary constituent of precipitates, Cu is only a small fraction of the precipitate chemistry, shown in the stacked bar chart for f.

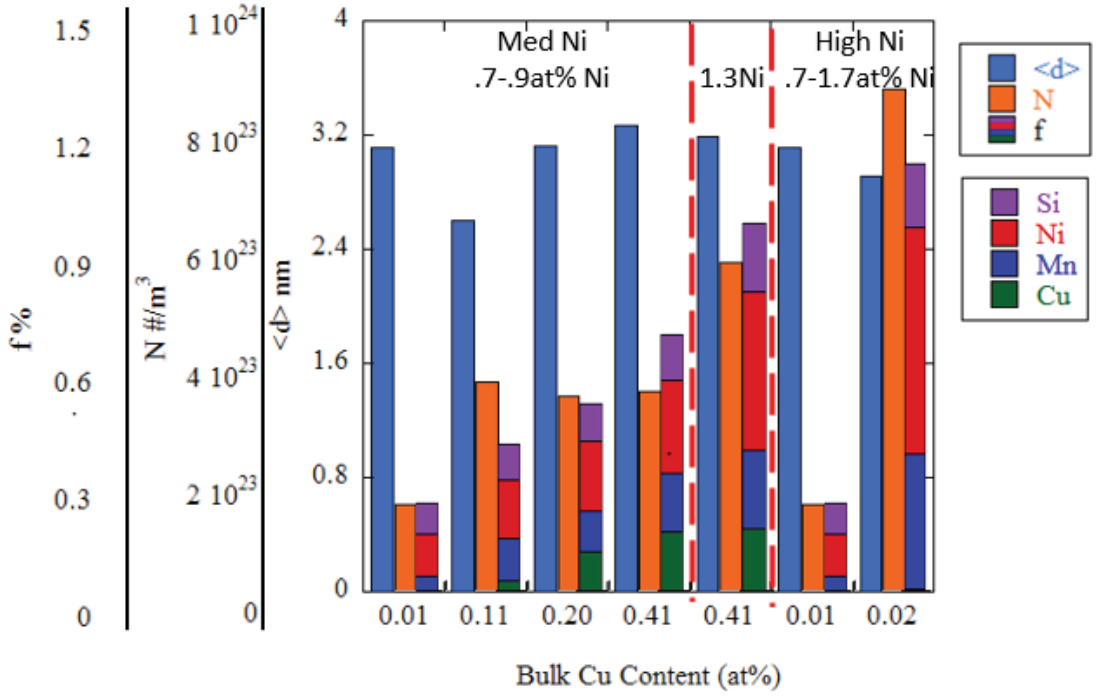

Figure 1 APT precipitate d, N and f as a function of measured bulk Cu and Ni content for the 6 core UCSB alloys irradiated in Cup 8. The f-bars show the Cu-Ni-Mn-Si precipitate compositions.

3.3 Morphology of Co-precipitated CRPs and MNSPs

The composition profiles and atom maps in Figure 4a and b (for the high Cu, high Ni alloy shown in Figure 2a and b, the CRPs first grow with a Cu-rich core-Mn-Ni-Si shell structure. The MNSPs later transform to CRPs with discrete ordered intermetallic appendages at high fluence. Figure 4c show blowups of CRP core-MNSP features, including an elongated appendage and a two-appendage dumbbell feature that are both thought to be characteristic of composite precipitates on dislocations as indicated by the presence of segregated P.

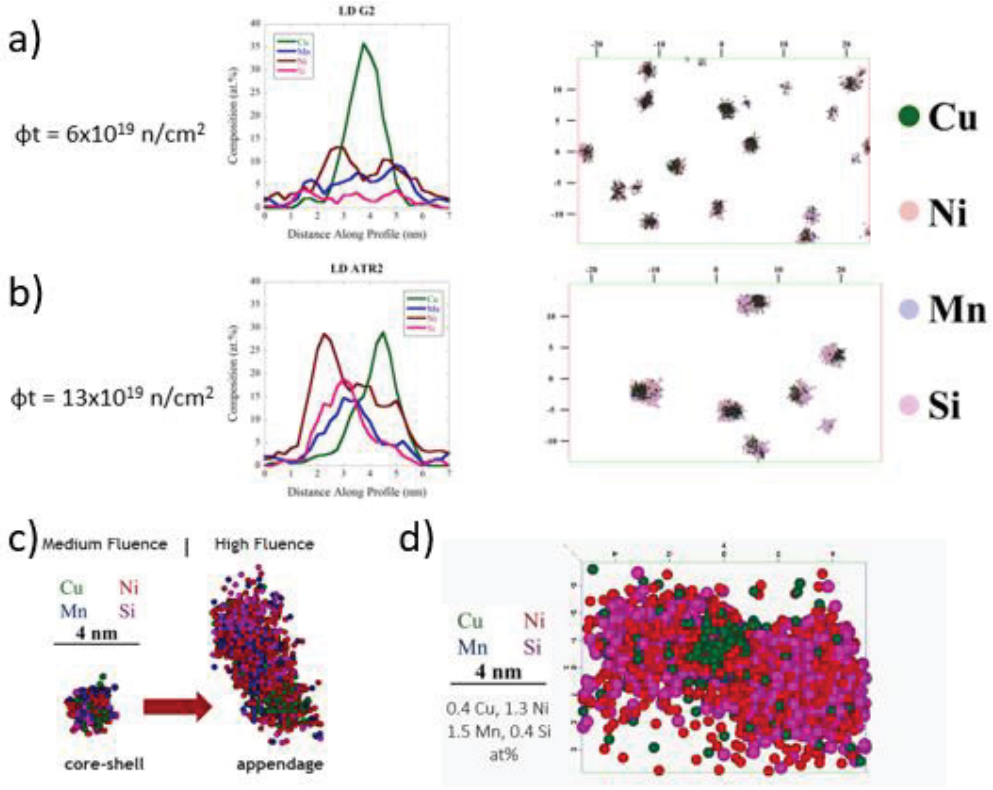

Figure 2 APT precipitate composition profiles and solute maps for a high 0.4at% Cu, high 1.3at% Ni steel (LD) at two ϕt: a) lower ϕt (G2: ϕt=6x10^{19} n/cm2) precipitates with CRP cores and MNS shells; b) higher ϕt (ATR-2: ϕt=13x10^{19} n/cm2) precipitates with CRP cores and MNS appendages. c) a blowup of precipitates with CRP cores and MNSP appendages.

3.4 Solute segregation and dislocation loops

As shown in Figure 5a, the Cu, Mn, Ni and Si solutes segregate to dislocations, including loops formed by irradiation. Figure 5b shows a blowup of a highly segregated loop containing a Cu precipitate. Larger loops are readily visible in low Ni steels, but are less obvious at higher Ni. It is likely that, in this case, the loops that form in cascades are still present, but are smaller and are further masked by segregation due to their immobilization by the segregated solutes that also provide elastic shielding of the dislocation cores. Examples of segregation to dislocation line and precipitation on line dislocation segments are shown in Figure 6. The concentration profile shows that the peak segregated concentrations of Mn, Ni and Si are very high, up to ≈ 5 at. %. Figure 7 shows that the precipitates heterogeneously form on dislocations at lower solute concentrations and higher temperatures (that is lower supersaturation).

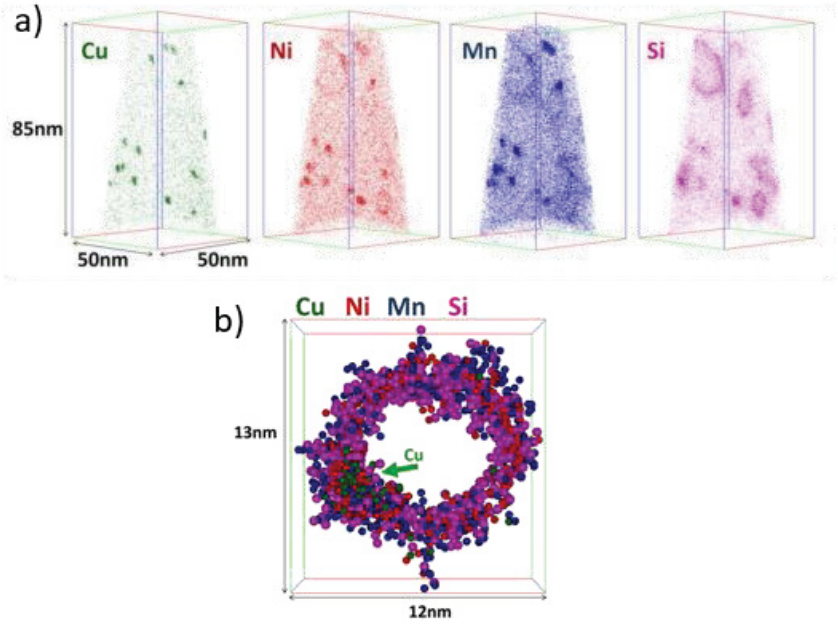

Figure 3 a) APT solute maps for a high (0.40%) Cu, low (0.18%) Ni steel (LB) showing a high density of dislocation loops decorated with solutes; and, b) an APT blowup of CRP on a dislocation loop with Mn-Ni-Si segregation.

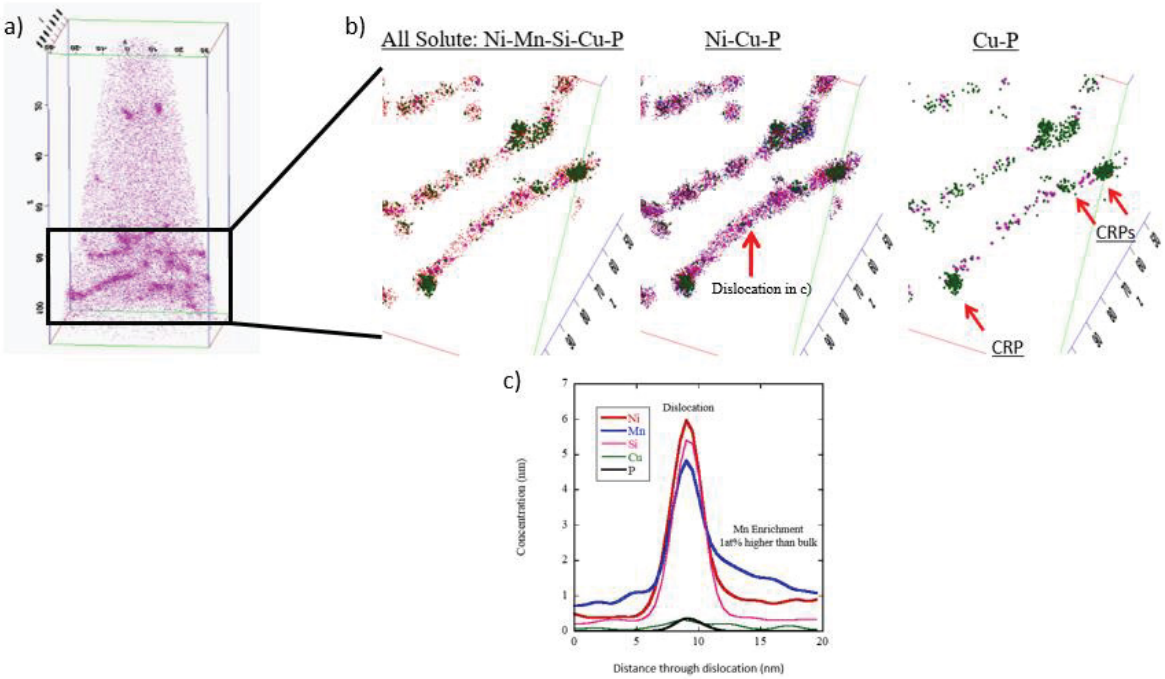

Figure 4 Med Cu (.1%) Med Ni (.75%) RPV steel (LH) a) APT Si atom map with Si segregation to dislocations; b) CRPs on dislocations showing segregation of all solute atoms, Ni-Cu-P , and Cu-P; c) Composition profile through dislocation from b) Local Mn concentration is 1at% higher in the region around dislocation than APT measured bulk.

Figure 7 APT solute maps of: a) a lower 0.11% Cu, medium 0.74 Ni RPV steel (LH) and, b) a (0.20%) higher 0.2% Cu medium 0.74% Ni RPV steel (LI) irradiated in IVAR to $\phi t \approx 1.7x10^{19}$ *n/cm*^{2} *and* $\phi \approx 0.33x10^{12}$ *n/cm*^{2}*-s at three different T. The precipitates all heterogeneously nucleate on dislocations in the lower Cu steel at all T and increasingly preferentially in the higher Cu steel with increasing T. (N. Soneda (CRIEPI) carried out the APT measurements as part of a collaboration with UCSB).*

3.5 *The Structure of the Precipitates*

X-ray diffraction (XRD) and Small Angle X-ray Scattering (SAXS) studies showed that the MNSPs in typical RPV steels are consistent with G-phase intermetallics and the X-ray results suggest that the Γ_2 phase was selected in one low (0.02%) Cu, high (1.70%) Ni steel (CM6)

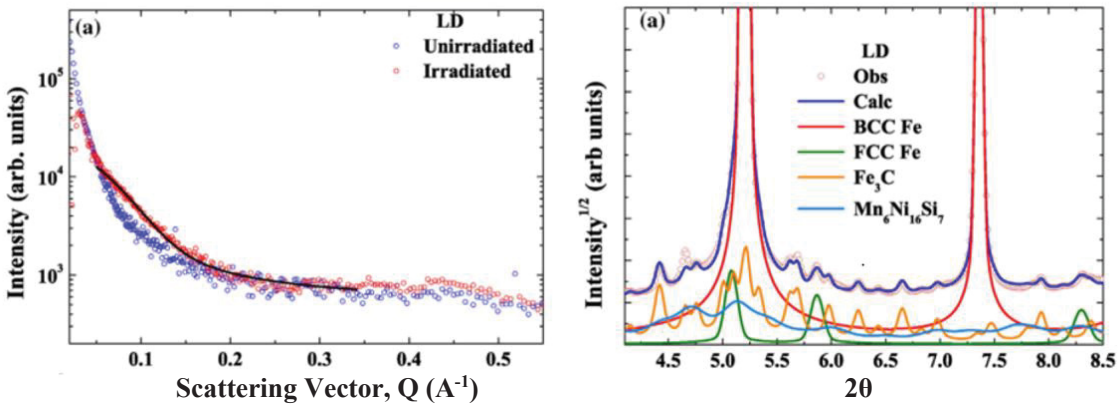

Figure 8 SAXS and XRD patterns for a high 0.4% Cu, high 1.3% Ni RPV steel (LD) irradiated at 320°C to 1.8 dpa in UCSB ATR-1. a) background corrected SAXS scattering intensity as a function of the scattering vector; and, b) a modified Rietveld refinement of the corresponding XRD pattern. The light blue curve identifies the G-phase structure.

Table 3 The SAXS and XRD results for the 6 core UCSB alloys from UCSB ATR-2 compared to APT and predicted phases from Calphad

Alloy ID	f (%)	d (nm)	XRD phase (Mn/Ni/Si)	APT (Mn/Ni/Si)	Calphad/TC Phase
LC	1.8 (0.2)	2.9 (fixed)	G (21/55/24)	37/44/19	G
LD	2.1 (0.2)	4.0 (fixed)	G (21/55/24)	25/52/23	G
LG	1.3 (0.2)	2.4 (fixed)	G (21/55/24)	31/46/23	G
LH	1.4 (0.2)	2.7 (fixed)	G (21/55/24)	37/43/20	G
LI	1.6 (0.1)	2.5 (fixed)	G (21/55/24)	35/44/21	G
CM6	2.9 (0.2)	3.2 (fixed)	Γ_2 (33/50/17)	35/53/12	Γ_2

Figure 9 shows an example SANS data on the Ni dependence of d, N and f for the low Cu alloys in for the 290°C irradiation (Cup 7 and 8) for alloys with containing more than 0.4 Si and 1.0 Mn, as is typical of RPV steels. While d is roughly constant, both N and f increase with increasing Ni. A similar trend is observed for the 255°C irradiation (Cup 5, not shown). Figure 10 shows that for the high > 0.2%Cu steels irradiated at 290°C, N and d do not show a systematic trend, but f again increases roughly linearly with Ni. Figure 11 shows that for alloys with < 1.4 Ni (to partly eliminate the strong Ni effect) d and f depend on strongly on Cu, but there is little effect on N. In summary, these results show that for the 290°C irradiation to $1.4x10^{20}$ n/cm^2, f increases with both Cu, due its effect on d, and Ni due to its effect on N. Although there are limited ASM data for the 255°C irradiation (Cup 5) there are similar trends for f with Ni at sufficiently high Mn. The effect of low Mn is discussed below.

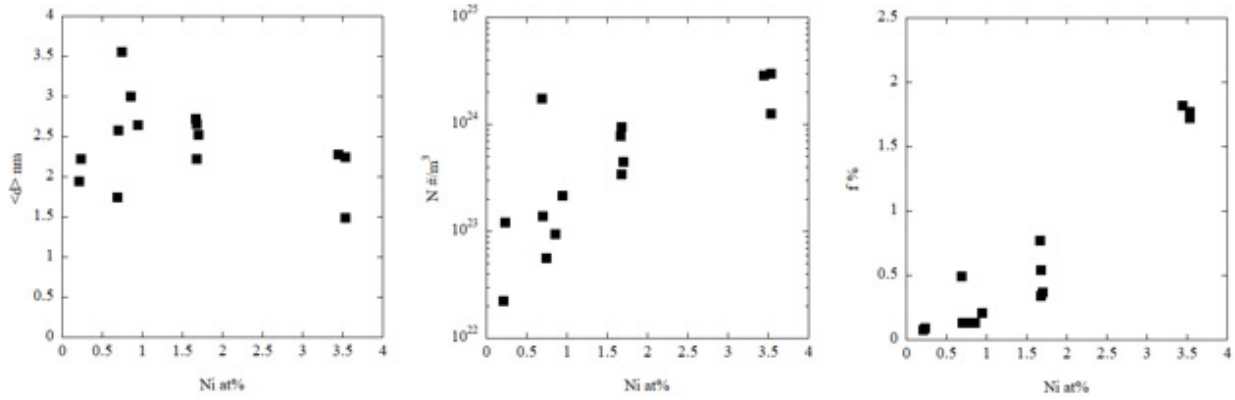

Figure 9 SANS <d> N and f Ni dependence for low (<.06%) Cu steels with >1.0%Mn and 0.40% Si irradiated at 290°C.

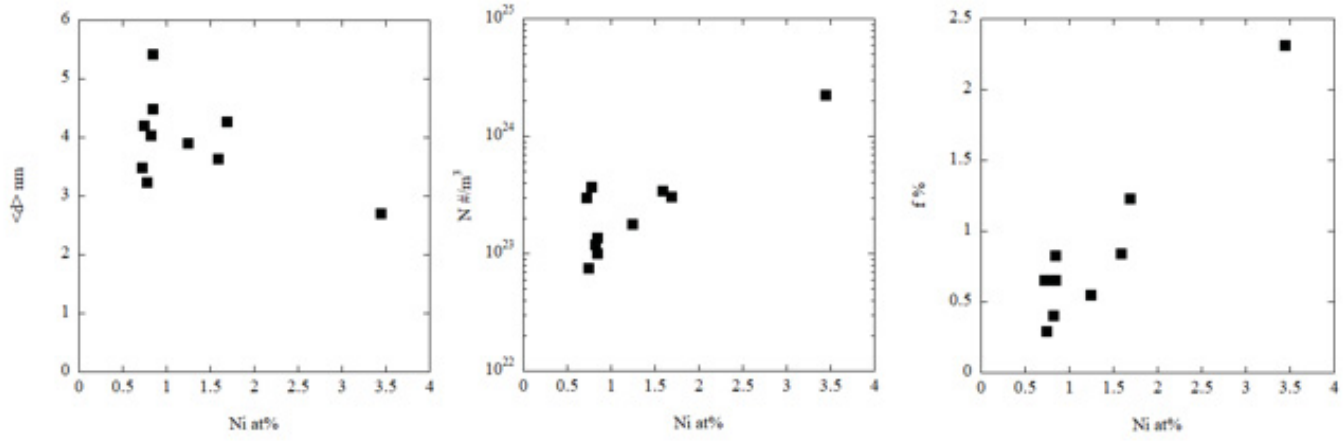

Figure 10 SANS <d> N and f Ni dependence of high (>.20%) Cu steels with >1.0%Mn and 0.40% Si irradiated at 290°C.

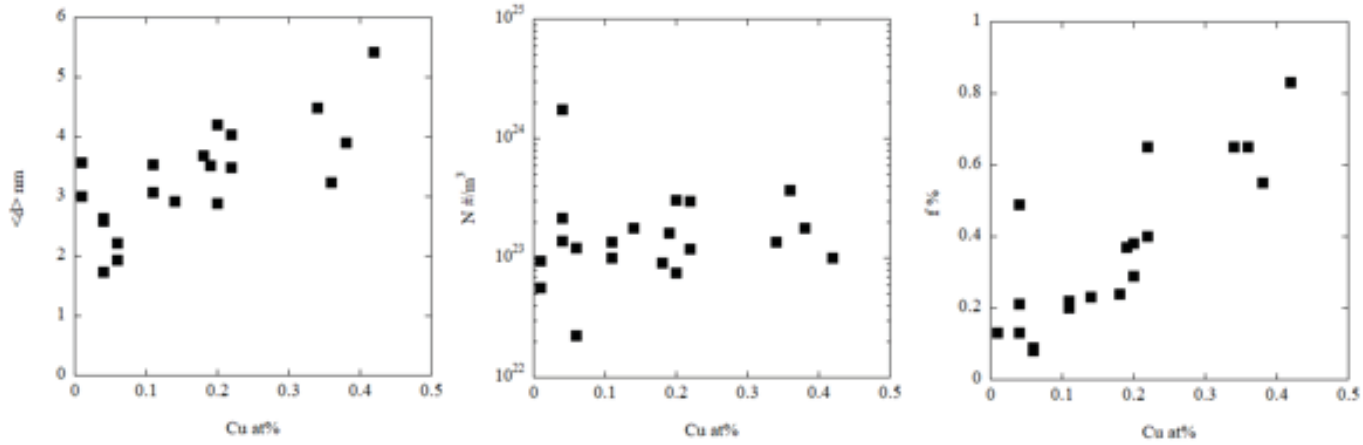

Figure 11 SANS <d> N and f Cu dependence for steels with <1.40% Ni, >1.0%Mn and 0.40% Si irradiated at 290°C.

The preceding results are based on SANS measurements. Note that, as shown in Figure 12, on average the f for SANS are only ≈ 2/3 of those measured by APT.

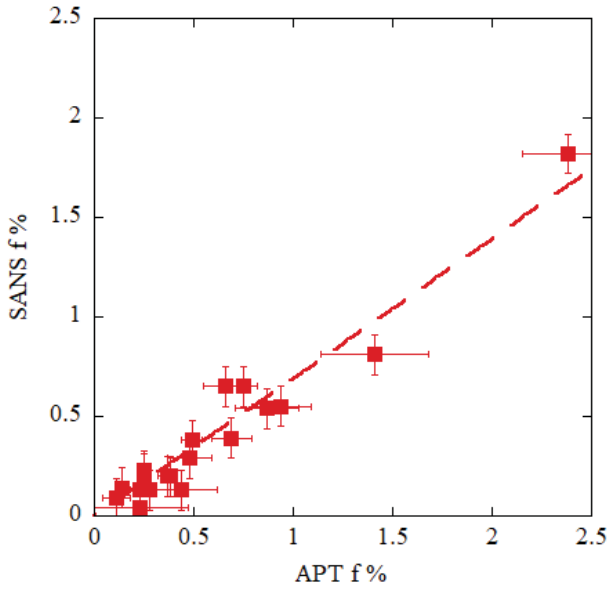

Figure 12 SANS versus APT f from ATR-2 for alloys irradiated at 290°C.

3.6 Alloy Composition and T Dependence of f – Dominance of Ni and Cu

Figure 13a shows that in low Cu steels, with typical amounts of Mn (> 1%), irradiated at 290°C, Ni primarily controls the MNSP f. Figure 13b shows a corresponding plot for Cu bearing steels where f roughly scales with 3Cu+Ni [or √f with √(3Cu + Ni)]. Similar dependence is observed at lower fluence in IVAR irradiations. However, at very high fluence of 1.4×10^{20} n/cm^2-s in the ATR- 1 irradiation, f scales with 2Ni + Cu. This is due to the fact that this irradiation condition produces nearly full precipitation and that both the G and Γ_2 phases have one (Si + Mn) atom for every Ni atom, coupled with the fact that Cu is nearly fully precipitates. Note these "eye-ball" chemistry factors are not optimized.

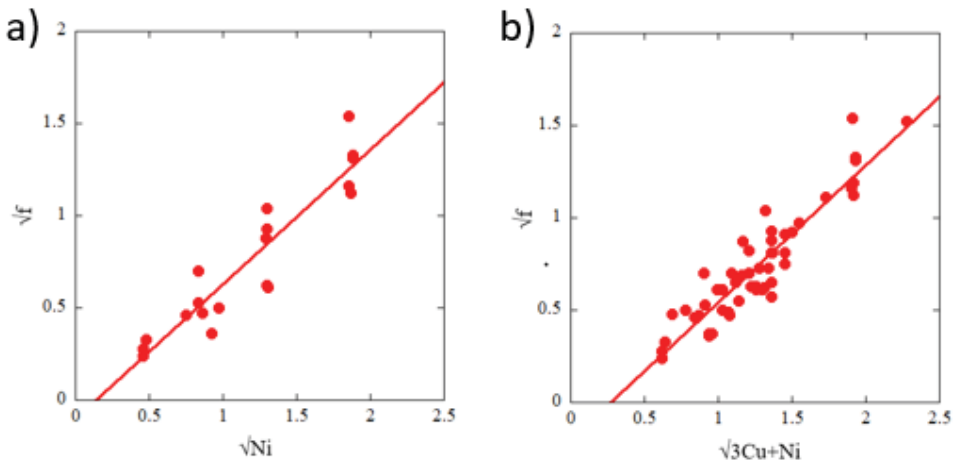

Figure 13 a) The √f as a function √Ni for low Cu (<.06%), >1% Mn steels irradiated at 290°C; and, b) the corresponding Square root of precipitate volume fraction as a function of the square root of 3Cu+Ni from low Cu (<.06%) >1% Mn steels irradiated at 290°C

SANS studies irradiations of advanced steel matrix (ASM) alloys with a much wider range of compositions at both 290 and 250°C show a very strong factor of 3 reduction in going from normal (1.5%) to very low Mn (0.25%) in a high Ni (3.5%) steel as seen in Figure 14. The corresponding effect of T is much weaker at ≈ 13% and 28%, for the normal versus low Mn, respectively, as seen in Figure 15. The strong effect of very low Mn there is an insufficient amount of this element to form the typical G and Γ_2 phases, thus the precipitates give way to Ni-silicides in steels with normal Si levels. The phase selection in the ASM alloy matrix is shown in Figure 16.

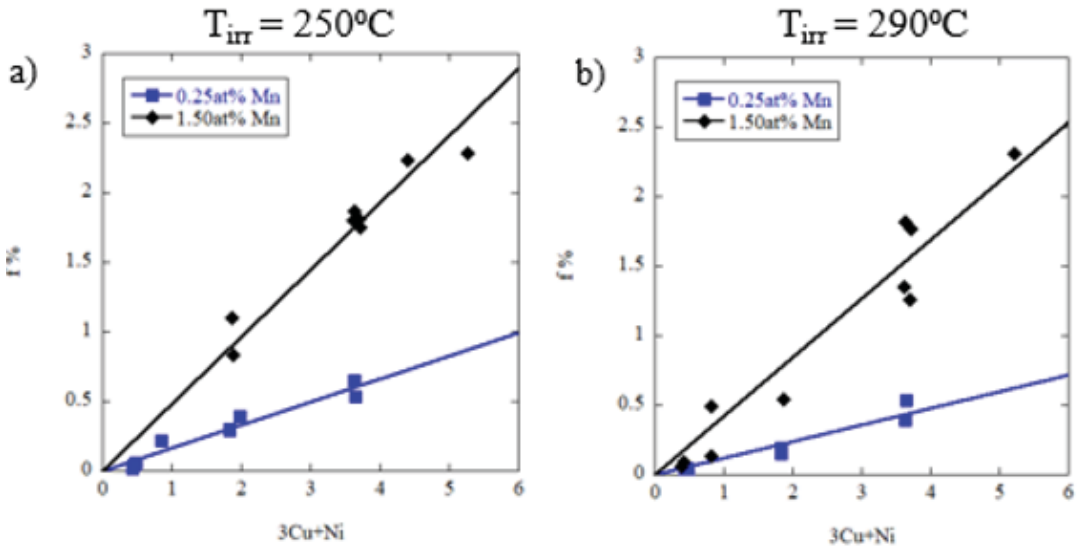

Figure 14 SANS f as a function of nominal bulk 3Cu+Ni from ASM alloys with 0.25% and 1.50% Mn) irradiated at 250°CC and 290°C

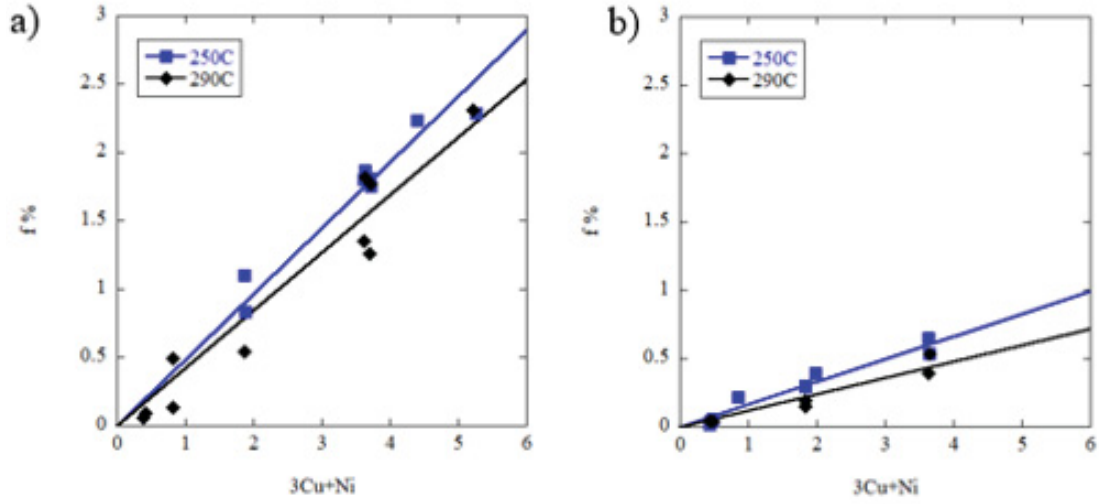

Figure 15 The same SANS f as a function of nominal bulk 3Cu+Ni for ASM for irradiations at 290C and 250C: a) 1.50% Mn); and, b) 0.25%.

Figure 17 shows that the total f in the ASM is generally insensitive to variations in Si and P at high fluence. Cu affects f for several reasons: even trace amounts of Cu promote MNSP formation; well-developed CRPs are heterogeneous nucleation sites for growing MNSPs; and, Cu nearly fully precipitates adding to the f from MNSPs.

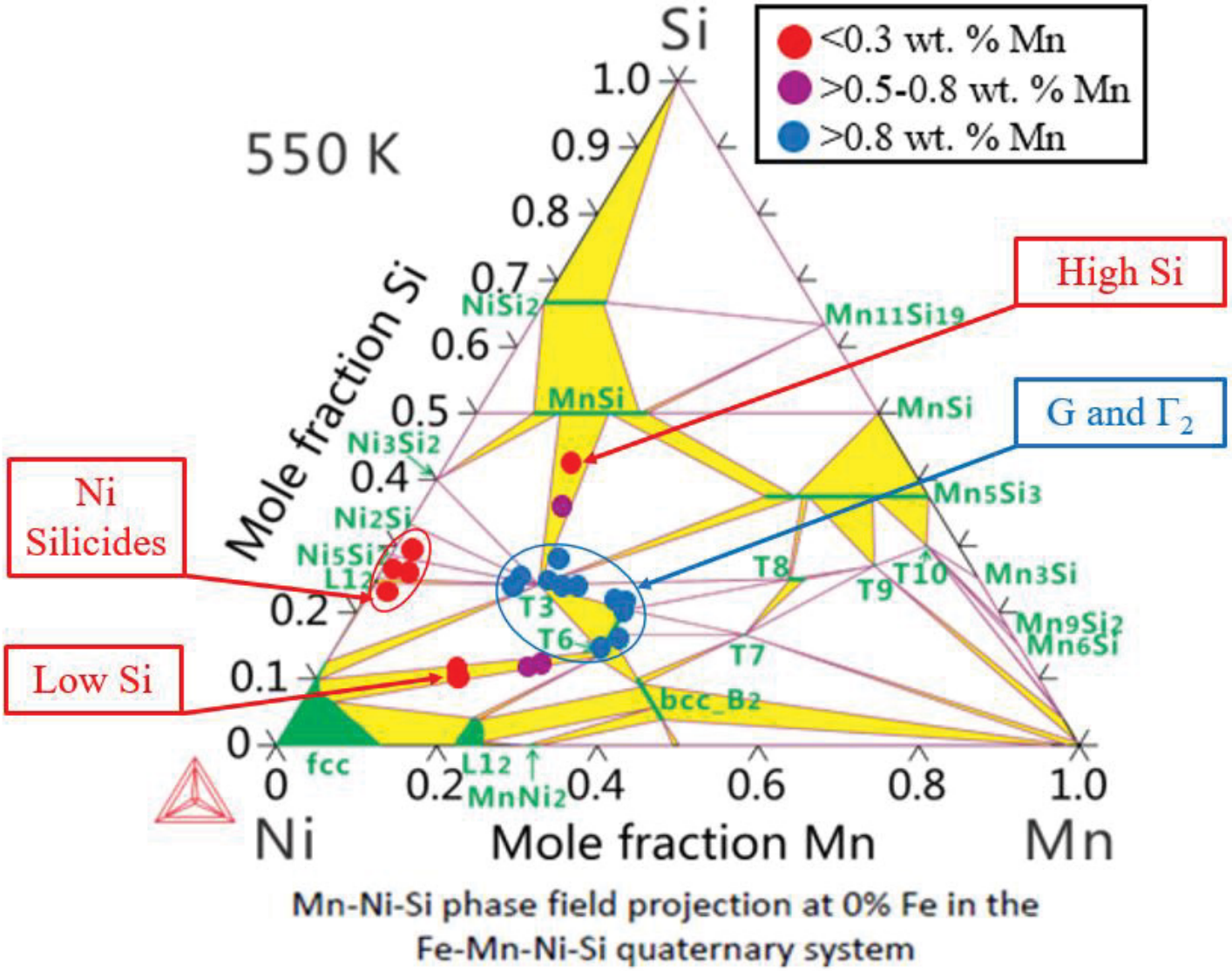

Figure 16 APT precipitate compositions for the ASM steels plotted on the Mn-Ni-Si ternary phase diagram.

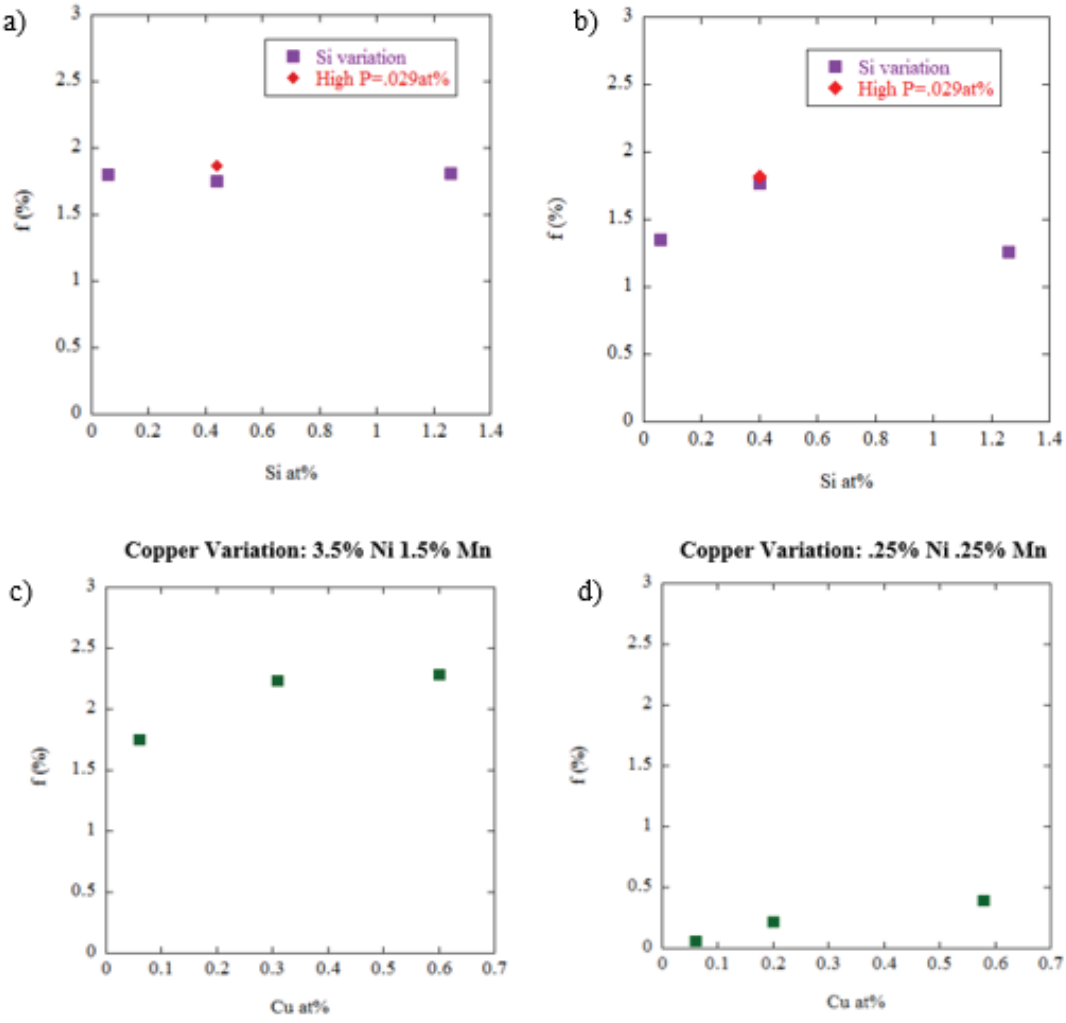

Figure 17 SANS f vs bulk Si for the ASM 3.5 Ni, 1.5 Mn alloys irradiated at: a) 255°C; b) 290°C; c) SANS f vs bulk Cu for a ASM 3.5%Ni, 1.5%Mn alloys; and, d) ASM 0.25%Ni, 0.25%Mn alloys.

3.7 Other APT Data

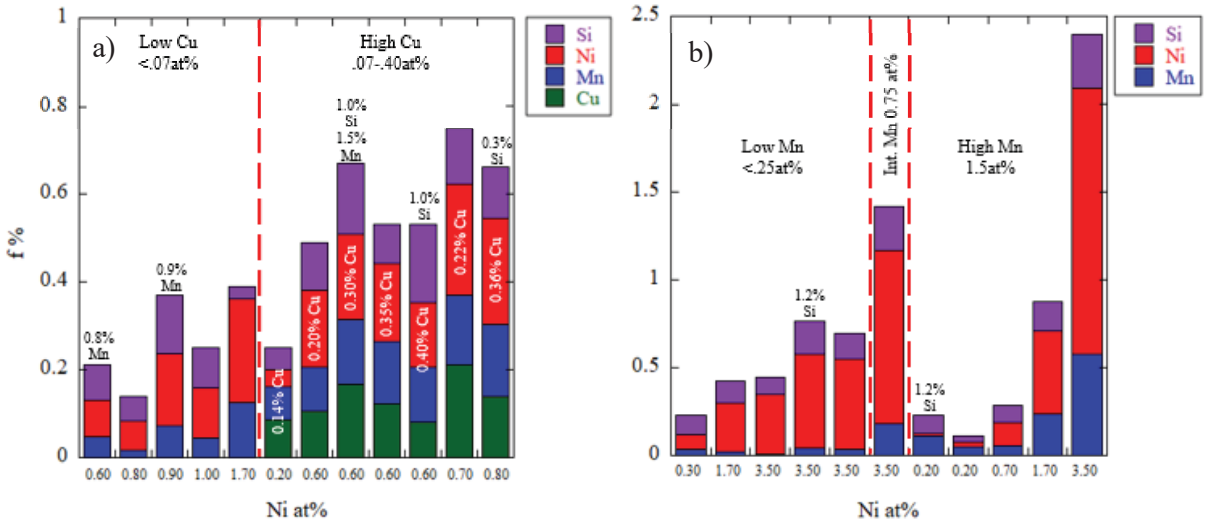

Figure 18 APT measured f and compositions of the: a) Surveillance and Program steels from the: a) 290°C irradiation; and, b) ASM steels from the 255°C irradiation. All alloys, unless marked, are < 0.07%Cu, >1% Mn and from 0.4-0.7% Si.

3.8 CRP and MNSP ϕt Dependence; Avrami Models for CRPs and MNSPs and a MNSP Precursor Model for SMF

It has been shown previously that Avrami models can be used to predict the CRP and MNSP f. However, this does not include the solute clustering in SMF that are important at low ϕt and are primarily composed of Mn, Ni and Si. Notably, the composition dependence of SMF hardening correlates with the alloy Mn, Ni and Si contents, roughly in similar proportions to the G-phase (≈ 2/1/1). However, it is difficult to observe low ϕt solute clusters since they are not yet well-formed MNSPs. Resistivity-Seebeck coefficient data shows solute clustering, with $f \approx 0.1\%$, in medium Ni steels at ≈ 1-3x10^{19} n/cm^2, but the results are uncertain and scattered. SANS suggests similar $f \approx 0.1$ values, at higher $\phi t \approx 10^{20}$ n/cm^2 and ϕ, but a similar effective ϕt_e. Limited low flux APT data on very low Cu steels in ϕt range from ≈ 1 to 5x10^{19} n/cm^2

finds a lower nominal f. But f increases linearly with ϕt and there is a high catalytic sensitivity to trace amounts of Cu, with $f \approx 4Cu$ (at $Cu < 0.07$) at a higher $\phi t \approx 10^{20}$ n/cm^2.

Here, we use the fact that $\Delta\sigma_y$ approximately correlates with $\sqrt{f}$ to infer lower fluence SMF solute clustering and precipitation behavior. Figure 19 plots $\Delta\sigma_y$ versus ϕt_e for low Cu, intermediate Ni (LG) and high Ni (CM6) alloys. The MNSP contribution to $\Delta\sigma_y(\phi t)$ (long dashed blue line) can be described by an Avrami model. For these purposes, the Avrami model is simply additively combined with a model for the SMF cascade solute-defect clusters (short dashed green line). The model assumes that the SMFs act as heterogeneous nucleation site precursors to MNSP. Thus the SMF hardening begins immediately at low ϕt, but subsequently peaks, decreases at still higher ϕt, as the SMFs transform to MNSPs and as the matrix is depleted of dissolved Mn, Ni and Si solutes reducing the rate of forming new SMFs. The combined Avrami MNSP and SMF model is consistent the hardening data over 5 orders of magnitude of ϕt and 3 orders of magnitude in ϕ.

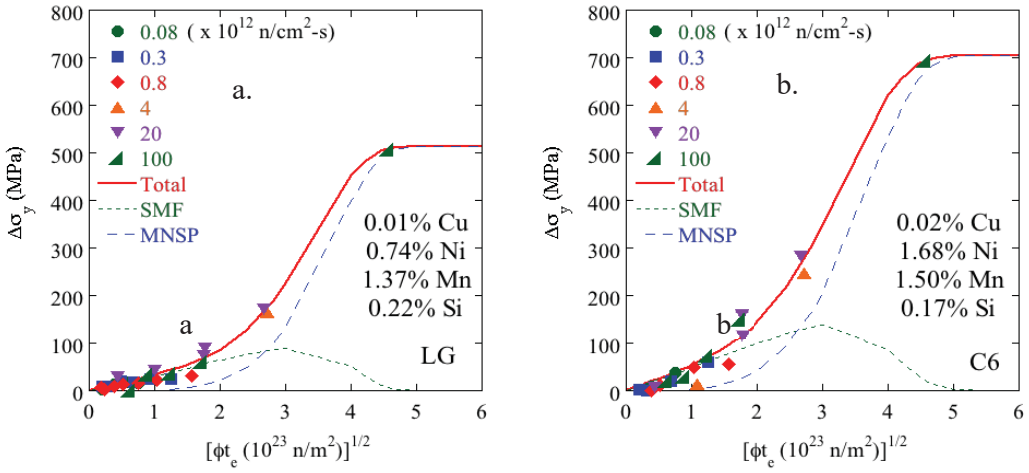

Figure 19 Hardening models for: a) low Cu (0.01%) medium Ni (0.74%) RPV steel (LG); and, b) low Cu (<0.06%) high Ni (1.70%) RPV steel (C6).

Figure 20, shows that the hardening in Cu-bearing steels can be described by two Avrami models for CRP (core) and MNSP (appendage) structures plus the SMF model, reasonably reflecting the corresponding ϕt dependence of √f.

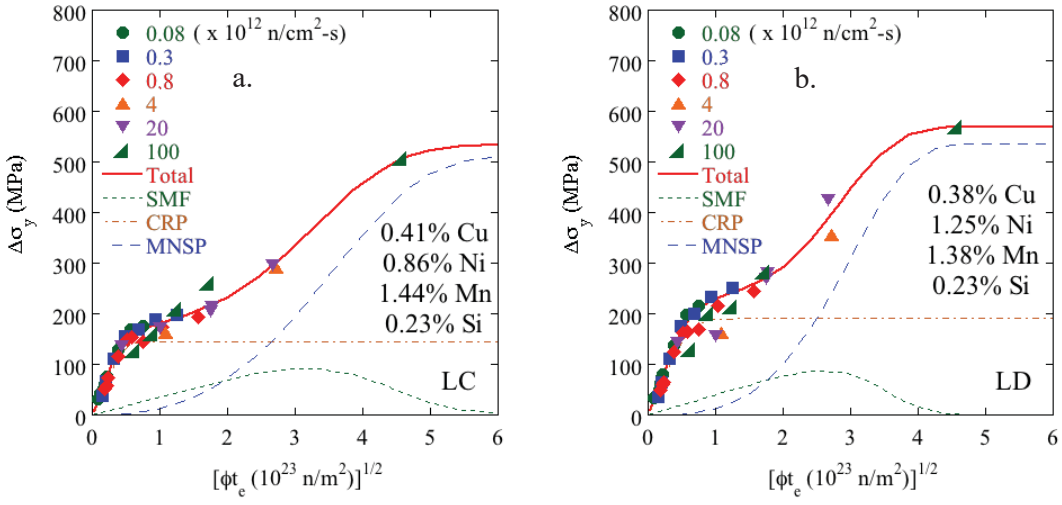

Figure 20 Hardening models for a) a high (0.41%) Cu, medium (0.86%) Ni steel (LC); and, b) high (0.38%) Cu, high (1.25%) Ni steel (LD).

3.9 Dose Rate Effects on Precipitate Evolution

The flux, or dose rate, effect can be understood and modeled in detail based on enhanced vacancy and self-interstitial atom recombination with increasing ϕ. Recombination decreases the excess vacancy concentration responsible for radiation-enhanced diffusion (RED) that greatly accelerates precipitation kinetics. Thus higher ϕt is required to reach the same total diffusion expressed in terms of a RED diffusion coefficient (D*) and time (t) as D*t. D* varies with ϕ to a power r (ϕ^r), that is less than 1 if recombination is significant. The irradiation time (t) varies with ϕ at a given fluences as t = ϕt/ϕ . Thus D*t at a specified ϕt scales as ϕ^{1-r} or ϕ^p,

at sufficiently low ϕ, when recombination rates are low and most defects are lost to sinks, p = 0 and there is no ϕ effect on RED kinetics. Note p can be even greater than 0.5 in some cases. There are other effects of flux that are beyond the scope of this discussion. The most salient point is that recombination is enhanced when vacancies are trapped at solutes characterized by a binding energy. Such solute enhanced recombination has been modeled and is a function of temperature, the defect sink strength (often taken as the dislocation density) and the concentration and vacancy binding energy of the solutes as illustrated in Figure 21 in terms of D*t/D*t (w/o recombination) versus ϕ. The ϕ–independent region at low ϕ (p=0) gives way to a recombination dominated region at high ϕ (p=0.5) Since there are other effects of flux and the model parameterization is not yet rigorous, we treat ϕt_e in terms of a simple scaling relation as $\phi t_e = \phi t[\phi r/\phi]^p$, where ϕr is an arbitrary reference ϕ and p is an empirical scaling exponent which is reasonably approximated as 0.25.

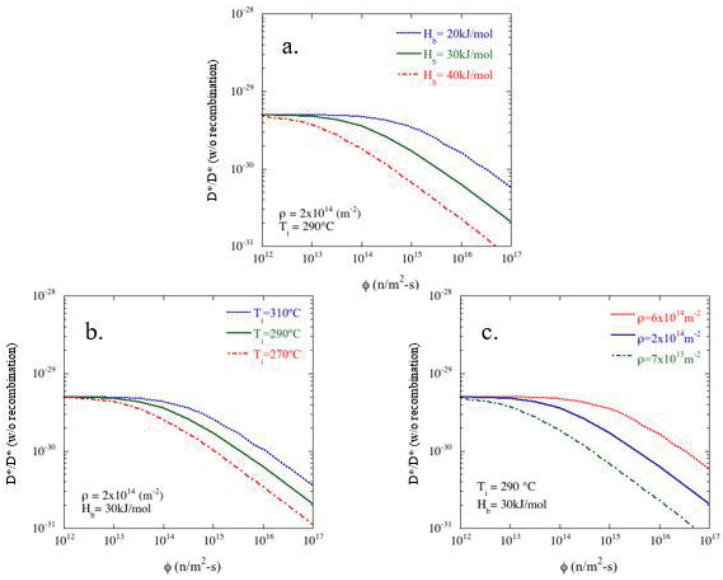

Figure 21 D/D* (w/o recombination as a function of ϕ for different: a) solute-vacancy binding energies; b) T; and, c) sink densities.*

Figure 22 shows f plotted against ϕt and ϕt_e for the 6 core alloys. assuming p= 0.25. The high, medium and low ϕ data are divided into broad bands respectively defined as high > 10^{13} n/cm^2-s, medium 10^{12}-10^{13} n/cm^2-s and low < 10^{12} n/cm^2-s. Clearly ϕte effectively removes the ϕ dependence that is obvious in the ϕt plots, except perhaps in the case of the high Ni alloy with the highest solute content.

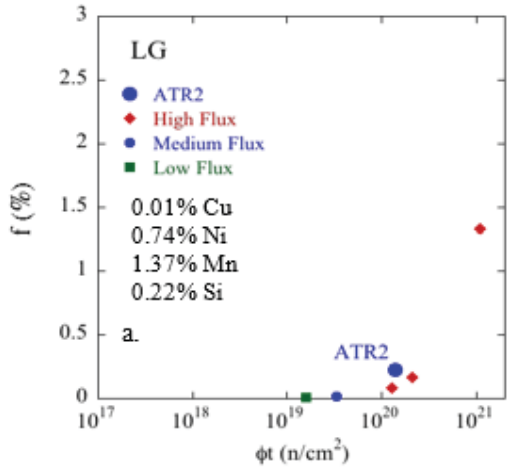
LG
ATR2
High Flux
Medium Flux
Low Flux
0.01% Cu
0.74% Ni
1.37% Mn
0.22% Si
a.
ATR2
f (%)
ϕt (n/cm²)

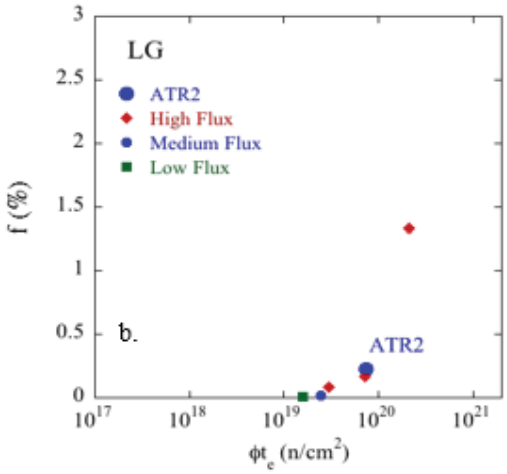
LG
ATR2
High Flux
Medium Flux
Low Flux
b.
ATR2
f (%)
ϕt_e (n/cm²)

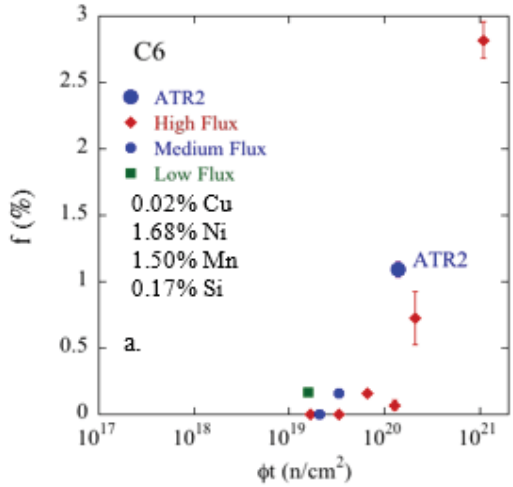
C6
ATR2
High Flux
Medium Flux
Low Flux
0.02% Cu
1.68% Ni
1.50% Mn
0.17% Si
a.
ATR2
f (%)
ϕt (n/cm²)

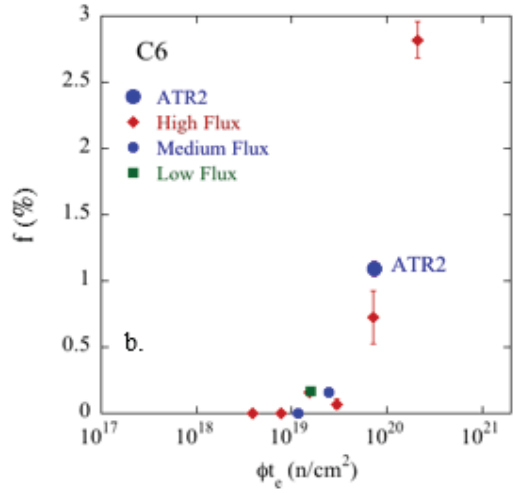
C6
ATR2
High Flux
Medium Flux
Low Flux
b.
ATR2
f (%)
ϕt_e (n/cm²)

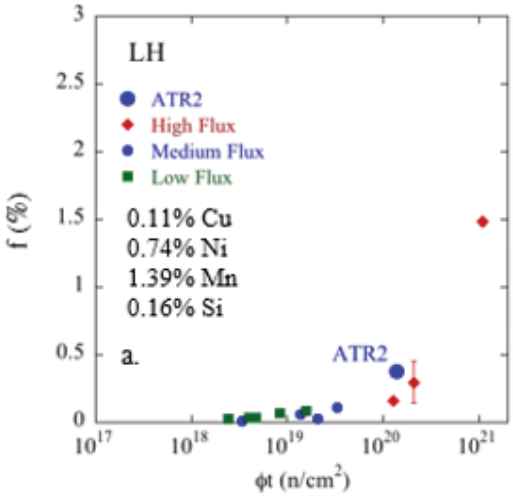
LH
ATR2
High Flux
Medium Flux
Low Flux
0.11% Cu
0.74% Ni
1.39% Mn
0.16% Si
a.
ATR2
f (%)
ϕt (n/cm²)

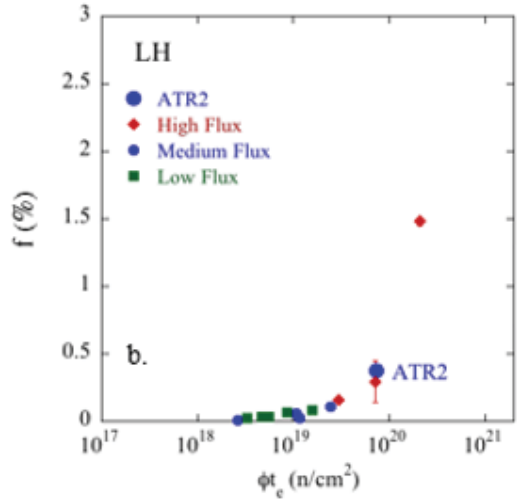
LH
ATR2
High Flux
Medium Flux
Low Flux
b.
ATR2
f (%)
ϕt_e (n/cm²)

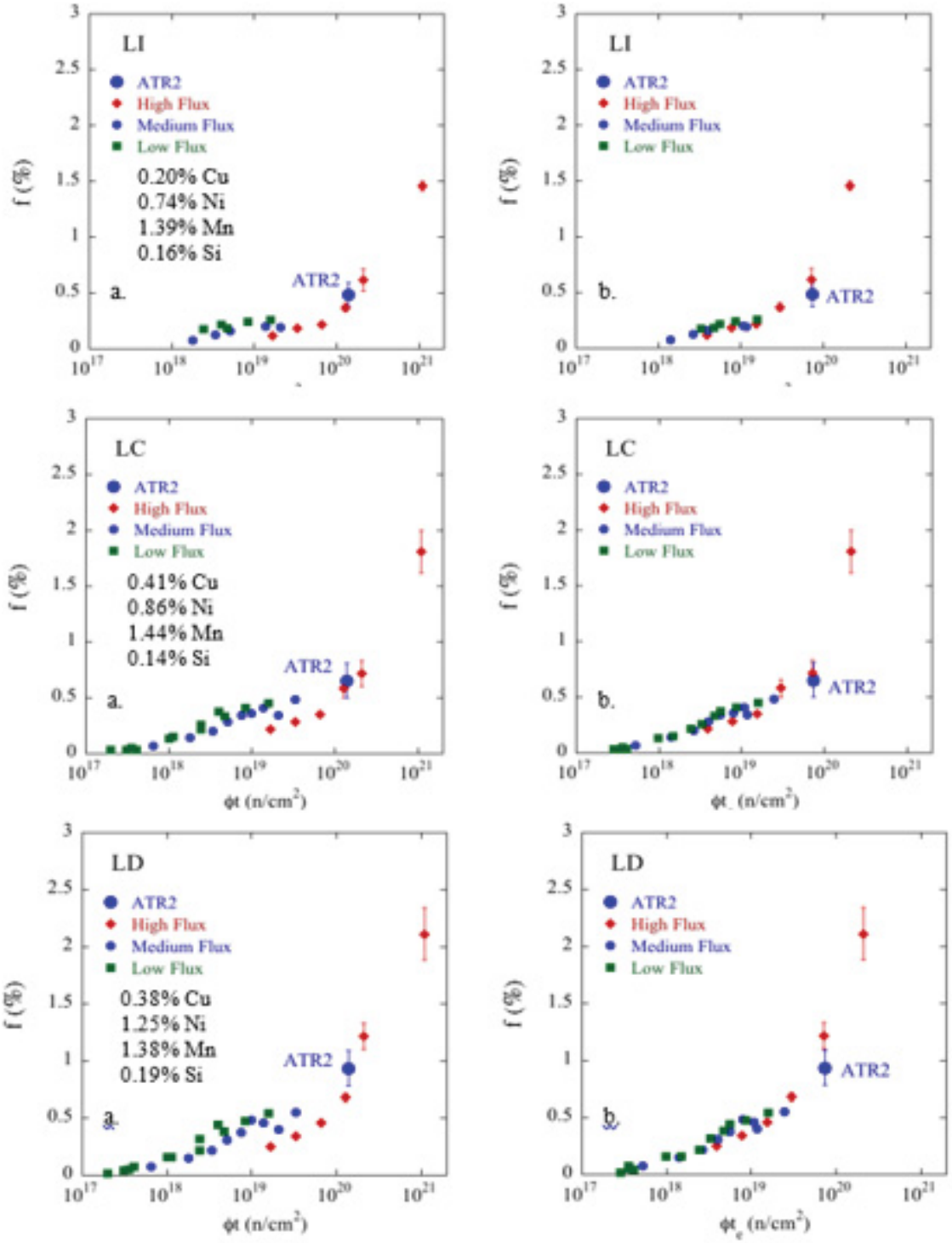

Figure 22 a) Evolution of f as a function of both ϕt (left) and ϕte (right) in three flux groups for the 6 UCSB core alloys for p = 0.25.

3.10 Ion Irradiations and Post Irradiation Annealing Studies

As seen in Figure 23, in the high dose nearly fully precipitated condition, high dpa rate ion irradiations produce CRPs and MNSPs that are similar to those found in ATR-1 neutron irradiated steels.

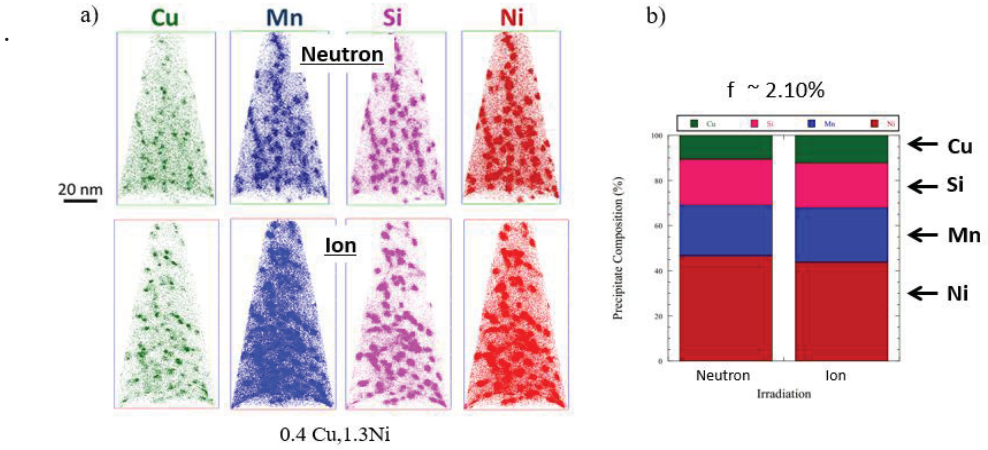

Figure 23 Comparisons of neutron (1.7 dpa) vs ion (4.2 dpa) precipitates in a high 0.4% Cu, high 1.3% Ni steel (LD): a) APT solute maps; and, b) the precipitate f and composition.

Post-irradiation annealing (PIA) studies at 425°C for up to 57 weeks show that the MNSPs in the high Ni steel are an equilibrium phases since the largest ones survive and begin to coarsen. However, as shown in Figure 24 the MNSP number densities decrease and the very small APT tip volume contains only a few precipitates at 57 weeks. The MNSP dissolution is due to the fact that small MNSPs are below the critical size in the solute depleted matrix, hence only the largest ones grow. The larger volume of material shown in the TEM EDS maps in Figure 25 (the TEM was carried out by Phil Edmonson at ORNL in collaboration with UCSB as part of a NSUF RTE experiment) shows more coarsened precipitates along with some very large Mn-Ni-Si rich features. The smaller features are essentially all associated with dislocations as shown by the dark field-EDS Ni overlay on the top right corner.

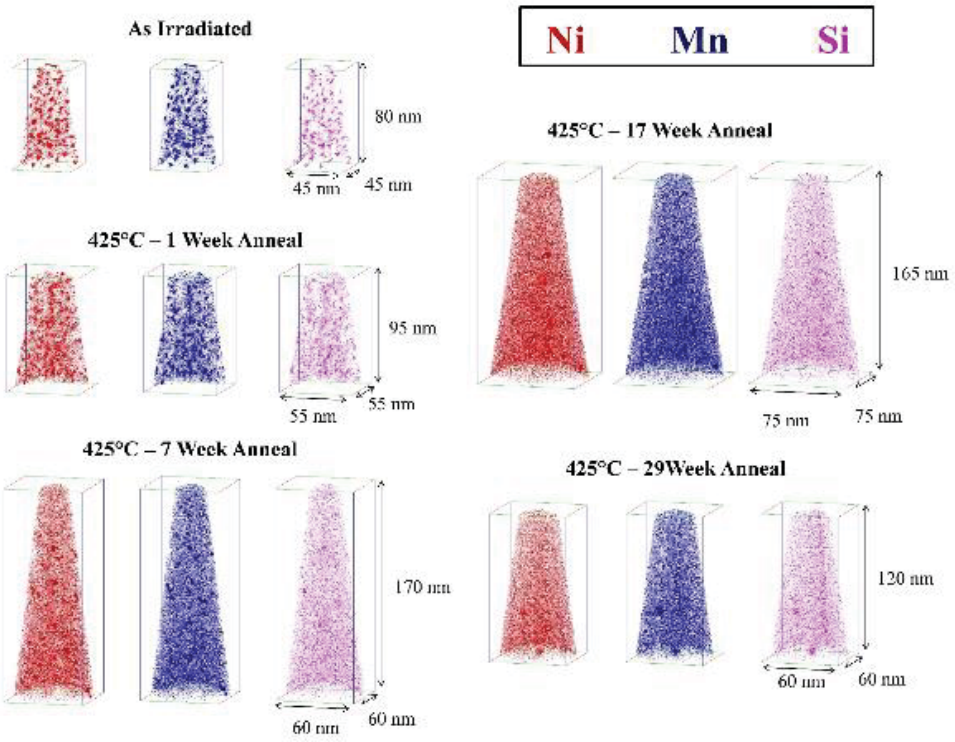

Figure 24 APT maps for the low 0.06% high 1.7% Ni steel (CM6) in the as-irradiated condition (top left) and 425C annealed conditions for times of: 1 (mid left), 7 (bottom left), 17 (top right) and 29 weeks (bottom right).

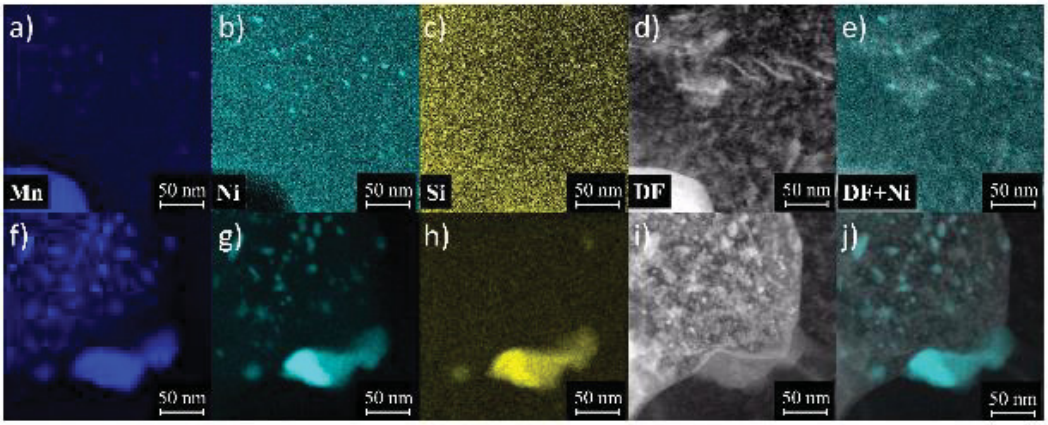

Figure 25 TEM EDS maps showing Mn-Ni-Si precipitates remaining in the high Ni steel CM6 after annealing for 57 weeks at 425°C (P. Edmondson).

To further test the hypothesis that the precipitates dissolved in the PIA study cited above because they were small and subject to the Gibbs-Thomson effect, 425°C anneals for up to 52 weeks we carried out following an ion irradiation that initially resulted in larger precipitates. The APT map in Figure 26 illustrates that these larger precipitates are much more stable than the smaller MNSPs in Figures 24 and 25. The larger volume EDS map in Figure 27 shows that a very high density of MNSPs remain after PIA, proving that they are equilibrium phases. Further, discussion of this very rich data set is beyond the scope of this report and will be reported in the future.

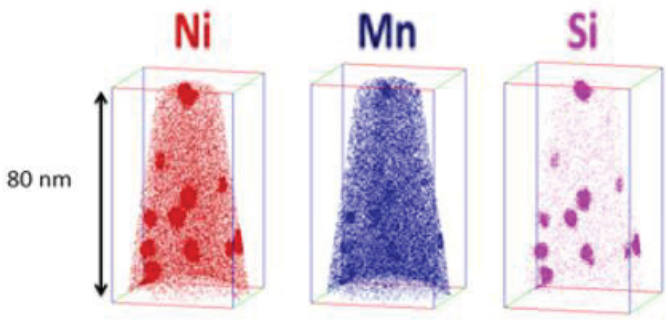

Figure 26 APT solute maps of a high Ni (1.7%) steel ion irradiated at 400C and annealed at 425C for 52 weeks.

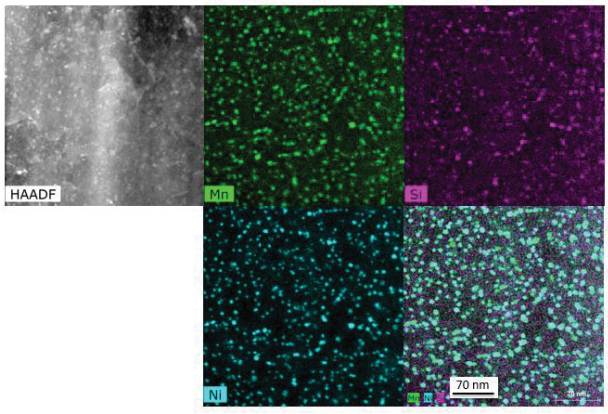

Figure 27 EDS maps showing Mn-Ni-Si a high density of MNSPs precipitates remaining in the high Ni steel, ion irradiated at 400C annealed for 52 weeks at 425°C.

3.11 The $\sqrt{f}$-$\Delta\sigma_y$ relation

Figure 28 plots $\Delta\sigma_y$ versus $\sqrt{f}$ for all the 327 data point pairs in our current databases. Although there are some highly scattered points, overall most data fall in a reasonably tight scatter band around the fitted polynomial shown as the solid line. The upward curvature is due to superposition effects of combining the unirradiated dispersed barrier hardening with dislocation pinning resulting by the precipitates. The dashed line a root sum square superposition for an Unirradiated obstacle contribution of 200 MPa and an isolated precipitate hardening contribution (if there was no other dispersed barrier hardening) of $\sigma_p \approx 428\sqrt{f(\%)}$ MPa.

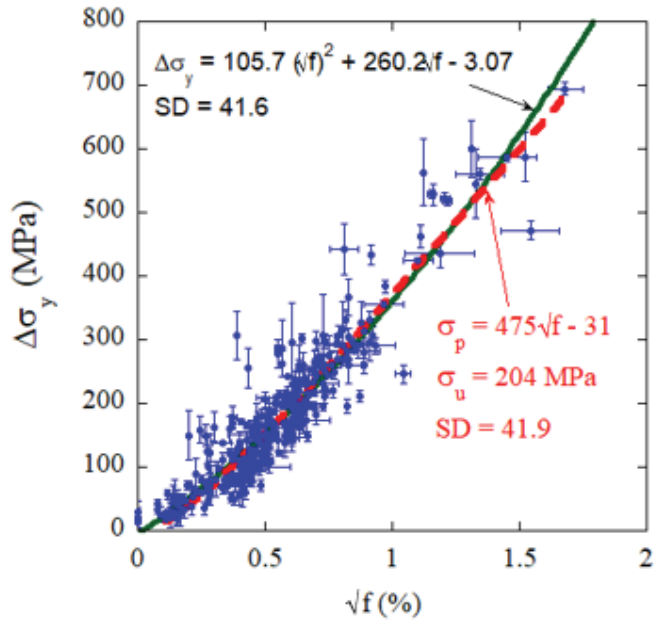

Figure 28 Irradiation hardening versus the square root of precipitate f for RPV steels from a subset of the UCSB database. The solid line is a polynomial fit and the dashed line is a root sum square superposition model as described in the text.

3.12 Support for Modeling Research

While outside the scope of this report it is important to note that the microstructural database we describe here has provided the foundation for the UW Madison-UCSB modeling collaboration as summarized in a recent report [8].

4. Brief Summary and Major Research Challenges

This report summarizes the status of UCSB's research on the microstructural basis for neutron irradiation embrittlement of RPV steels. We derive a number of conclusions from our comprehensive and unique results to date, that paint a striking picture of the causes and consequences of the evolution of both nanoscale Cu-rich and Mn-Ni-Si late blooming precipitates. The MNSPs form in all steels, but are mainly driven by Cu (CRPs) and Ni (MNSPs) at the ATR-2 ϕt of $\approx$ 1.3-1.4x10^{20} n/cm^2 at 250 and 290°C. At normal RPV steel Mn levels, even in low Cu steels the mole fraction of MNSPs increases with Ni up to f of several percent at ATR-2 the irradiation conditions. However, the f is much less in steels with very low Mn, where MNSPs give way to Ni silicide phases. In Cu bearing steels, CRPs quickly form, and MNSPs subsequently grow as intermetallic appendices on the Cu rich core-Mn-Ni-Si shell structures. Significant segregation to dislocations is observed, including loops, and this may play a critical role in nucleation CRPs and MNSPs, especially at lower solute contents and higher temperatures (that is, at lower supersaturation). While not fully quantified yet, our overall microstructural database provides a robust, fundamental foundation to develop ϕt and composition models of precipitation and the corresponding hardening and embrittlement.

The ATR-2 extends our microstructural database to ϕt levels characteristic of extended life RPV operation to 80 years or more. Integration of ATR-2 with our other databases, that span

3 and 4 orders of magnitude in ϕ and ϕt, respectively, will allow us to address the challenge of fully quantifying dose rate effects in embrittlement models applied to extended life RPV service conditions. This is a major research challenge that will be the focus of our ongoing research.

5. References

1. Odette GR, Yamamoto T, Wells PB, Almirall N, et al. "Update on the ATR-2 Reactor Pressure Vessel Steel High Fluence Irradiation Project", 2016;UCSB ATR-2 2016-1.
2. Odette GR, Yamamoto T, Wells PB, Almirall N, et al. "Summary of Progress on the ATR-2 Experiment Post-Irradiation Examination of Reactor Pressure Vessel Alloys", 2017; UCSB ATR-2 2017-1
3. Eason ED, Odette GR, Nanstad RK and Yamamoto T. "A physically based correlation of irradiation-induced transition temperature shifts for RPV steels," Oak Ridge National Lab, 2007; ORNL/TM-2006/530.
4. ASTM E900-02, Standard Guide for Predicting Radiation-Induced Transition Temperature Shift for Reactor Vessel Materials, Annual Book of ATSM Standards, vol. 12.02 (West Conshohocken, PA: American Society for Testing and Materials)
5. Wells PB, Yamamoto T, Miller B, Milot T, et al. "Evolution of manganese–nickel–silicon-dominated phases in highly irradiated reactor pressure vessel steels", *Acta Mater.* 2014;80:205–219.
6. "As-Run Thermal Analysis of the UCSB-2 Experiment in the ATR," 2016; ATR NSUF ECAR No. 3218, Project No. 30946.
7. "As-Run Physics Analysis for the UCSB-2 Leadout Experiment in I-22," 2016; ATR NSUF ECAR No. 3219, Project No. 30946.
8. Morgan D, Shipeng S, Mamivand M, Huibin K, et al. "Complete report that documents the completion of a validated model for transition temperature shift in RPV steels", 2017;UM, 2017-2